Distributed Aberration Correction in Handheld Ultrasound Based on Tomographic Estimates of the Speed of Sound

Rehman Ali[1,2,*], Trevor Mitcham[1,3,*], Melanie Singh[1,4], Richard Bouchard[3], Jeremy Dahl[2], Marvin Doyley[5], and Nebojsa Duric[1]

[1]Dept. of Imaging Sciences, Univ. of Rochester Medical Center, Rochester, NY, USA
[2]Dept. of Radiology, Stanford School of Medicine, Palo Alto, CA, USA
[3]Dept. of Imaging Physics, Univ. of Texas MD Anderson Cancer Center, Houston, TX, USA
[4]Dept. of Biomedical Engineering, Univ. of Rochester, Rochester, NY, USA
[5]Dept. of Electrical and Computer Engineering, Univ. of Rochester, Rochester, NY, USA
[*]These authors contributed equally to this work

ABSTRACT

Phase aberration is one the key sources of image degradation in handheld B-mode ultrasound imaging. Sound speed heterogeneities create phase aberrations in the image by inducing additional tissue-dependent delays and diffractive effects that conventional beamforming does not incorporate. For this reason, the Fourier split-step angular spectrum method is used to simulate pressure fields in a heterogeneous sound speed medium and create B-mode images based on the cross-correlation of transmitted and received wavefields. Because the strongest aberrations are caused by a laterally varying sound speed profile, this work presents a new sound speed estimator that can be used to correct for aberrations in laterally varying media. Phantom experiments show a 58-76% improvement in point target resolution and a 2.5x improvement in contrast-to-noise ratio because of the proposed sound speed estimation and phase aberration correction scheme.

Keywords: Nonlinear inverse problems, pulse-echo ultrasound, reflection tomography, aberration correction, speed-of-sound imaging, Fourier split-step migration, time-shift gathers, lag-one coherence

1. INTRODUCTION

While many methods exist for phase aberration correction, they often fall short in many practical scenarios. For instance, phase screen models such as the near-field phase screen,[1–3] or the midfield phase screen,[4,5] assume that all of the aberration in image can be explained by time shifts introduced at a single thin film. Other approaches such as the time-reversal mirror[6] can be used to optimally focus the imaging target regardless of the sound speed distribution in tissue, but they require a physical retransmission of received ultrasound signals back into the tissue to optimally focus the imaging target. This requires real-time arbitrary waveform generation which remains infeasible for most commercial ultrasound systems to this day.

Although deviations in sound speed were always understood as the mechanism behind aberration in ultrasound imaging, the modeling and correction of aberration remained limited to the aforementioned phase screen models and time reversal approaches until recent efforts to directly reconstruct the sound speed profile in tissue from phase aberrations.[7–9] These works motivated a new set of approaches to correct for aberrations in the image based on knowledge of the sound speed profile in the tissue.[10–14] A major limitation identified in recent works[15,16] is that the average sound speed or depth-wise variation in sound speed falls in the null-space of the aberration delay measurement process. In other words, the reflection tomography described in prior works[7–9] would not be able to accurately recover a bulk error in sound speed. Instead, reflection tomography is more likely to estimate a near-field disturbance that compensates for a bulk error in sound speed.

Currently, the sound speed estimators that can accurately reconstruct the bulk or depth-varying sound speed profile are only suitable for layered media.[11,17] The purpose of this work is to develop a method of sound speed

Further author information: (Send correspondence to Rehman Ali)
Rehman Ali: E-mail: rali8@stanford.edu

Medical Imaging 2023: Ultrasonic Imaging and Tomography, edited by Christian Boehm, Nick Bottenus, Proc. of SPIE Vol. 12470, 1247009

· 1605-7422 · doi: 10.1117/12.2653935

estimation and aberration correction that relies on improvements in the aberration delay measurement process to yield sufficiently accurate sound sound estimates that enables B-mode imaging with improved resolution and quality in complex aberrating media. Our previous work on sound speed estimation and phase aberration correction were primarily limited to layered media with small lateral variations in the speed of sound.[11] Unfortunately, this prior work showed the degradation of sound speed estimation and phase aberration correction in the presence of large lateral variations in the speed of sound. In contrast, this work replaces the previous sound speed estimator with a new approach that better accounts for aberrations resulting from lateral variations in the speed of sound. These improvements come at the cost of measuring a potentially incorrect global average or depth-varying sound speed profile as previously shown in the literature.[15,16]

2. METHODS

2.1 Fourier Split-Step Angular Spectrum Method

Ultrasonic wave-fields $p(x, z, f)$ as a function of location (x, z) and frequency f can be propagated from a depth of z to $z + \Delta z$ using the Fourier split-step method[11,13,14,18]

$$p(x, z + \Delta z, f) = W(x) S_{\pm}(x, z, f) \mathcal{F}^{-1}_{k_x \mapsto x} H_{\pm}(k_x, z, f) \mathcal{F}_{x \mapsto k_x} p(x, z, f), \tag{1}$$

$$H_{\pm}(k_x, z, f) = \exp\left(\pm j 2\pi \left(\frac{f^2}{\bar{c}^2(z)} - k_x^2 \right)^{1/2} \Delta z \right), \tag{2}$$

$$S_{\pm}(x, z, f) = \exp\left(\pm \frac{j 2\pi f \Delta z}{c_{res}(x, z)} \right), \tag{3}$$

$$\frac{1}{\bar{c}(z)} = \frac{1}{L} \int_{-L/2}^{L/2} \frac{dx}{c(x, z)}, \tag{4}$$

$$\frac{1}{c_{res}(x, z)} = \frac{1}{c(x, z)} - \frac{1}{\bar{c}(z)}. \tag{5}$$

where $\mathcal{F}_{x \mapsto k_x}$ and $\mathcal{F}^{-1}_{k_x \mapsto x}$ are the forward and inverse Fourier transforms in the lateral dimension (x), $W(x)$ is an anti-aliasing window used to suppress wrap-around in the lateral dimension, $c(x, z)$ is the sound speed in the medium as a function of (x, z), and L is the lateral length of the computational domain over which the angular spectrum method is applied. Because this is a Fourier split-step scheme, we decompose $c(x, z)$ into an axially-varying component $\bar{c}(z)$ and a laterally varying component $c_{res}(x, z)$.

2.2 Imaging by Correlation of Transmit and Receive Wavefields

Pulse-echo ultrasound images can be created by propagating transmit and receive wavefields $p_{tx(i)}(x, z, f)$ and $p_{rx(i)}(x, z, f)$ based on the receive channel data collected from pulses emitted by each transmit element $i = 1, ..., N$. Partial images $I_i(x, z)$ can be formed prior to amplitude detection based on the following equations:

$$I_i(x, z) = \int_0^{\infty} p^*_{tx(i)}(x, z, f) p_{rx(i)}(x, z, f) df, \tag{6}$$

$$p_{tx(i)}(x, z + \Delta z, f) = W(x) S_{-}(x, z, f) \mathcal{F}^{-1}_{k_x \mapsto x} H_{-}(k_x, z, f) \mathcal{F}_{x \mapsto k_x} p_{tx(i)}(x, z, f), \tag{7}$$

$$p_{rx(i)}(x, z + \Delta z, f) = W(x) S_{+}(x, z, f) \mathcal{F}^{-1}_{k_x \mapsto x} H_{+}(k_x, z, f) \mathcal{F}_{x \mapsto k_x} p_{rx(i)}(x, z, f), \tag{8}$$

2.3 Aberration Delay Measurements Using Time-Shift Gathers

Equation 6 is augmented to include a time axis t using the concept of time-shift gathers:[19]

$$I_i(x, z; t) = \int_0^{\infty} p^*_{tx(i)}(x, z, f) p_{rx(i)}(x, z, f) e^{j 2\pi f t} df. \tag{9}$$

The aberration delay t_d between I_i and I_{i+1} at each point (x, z) is found by maximizing the time-domain correlation between $I_i(x, z; t)$ and $I_{i+1}(x, z; t - t_d)$.

2.4 Apodization that Maximizes the Correlation between I_i and I_{i+1}

We define the lag-one coherence (LOC)[20] optimal apodization as the receive apodization that maximizes the correlation between echoes imaged by neighboring single-element transmissions (I_i and I_{i+1}) from the array. Applying the principle of acoustic reciprocity to the van-Cittert Zernike (VCZ) theorem,[?] the correlation between neighboring transmit channels is the lag-one autocorrelation of the receive apodization. Given a vector of apodization weights $\vec{w} = [w_1, ..., w_N]^T$ for an N-element transducer, its autocorrelation ρ_n at lag n is

$$\rho_n = \vec{w}^T A_n \vec{w}, \tag{10}$$

where A_n is a matrix where the n^{th} diagonal is all ones and remaining entries of the matrix are zero (e.g., A_0 is the identity matrix, A_1 only has ones on the first superdiagonal, and A_{-1} only has ones on the first subdiagonal):

$$A_0 = \begin{bmatrix} 1 & 0 & & 0 \\ 0 & 1 & \ddots & \\ & \ddots & \ddots & 0 \\ 0 & & 0 & 1 \end{bmatrix}, \quad A_1 = \begin{bmatrix} 0 & 1 & & 0 \\ 0 & 0 & \ddots & \\ & \ddots & \ddots & 1 \\ 0 & & 0 & 0 \end{bmatrix}, \quad A_{-1} = \begin{bmatrix} 0 & 0 & & 0 \\ 1 & 0 & \ddots & \\ & \ddots & \ddots & 0 \\ 0 & & 1 & 0 \end{bmatrix}. \tag{11}$$

Note that $\rho_n = \rho_{-n}$. The optimal apodization should minimize $\rho_0 - \rho_1$ subject to the constraint that $\|\vec{w}\| = 1$. To ensure the symmetric positive definiteness of this optimization problem, $2\rho_0 - \rho_1 - \rho_{-1}$ is minimized instead:

$$\begin{aligned} \underset{x}{\text{minimize}} \quad & 2\rho_0 - \rho_1 - \rho_{-1} = \vec{w}^T(2A_0 - A_1 - A_{-1})\vec{w}, \\ \text{subject to} \quad & \vec{w}^T\vec{w} = \sum_{n=1}^{N} w_n^2 = 1. \end{aligned} \tag{12}$$

where $2A_0 - A_1 - A_{-1}$ is simply a tri-diagonal toeplitz matrix with diagonals $[-1, 2, -1]$:

$$2A_0 - A_1 - A_{-1} = \begin{bmatrix} 2 & -1 & & 0 \\ -1 & 2 & \ddots & \\ & \ddots & \ddots & 1 \\ 0 & & -1 & 2 \end{bmatrix}. \tag{13}$$

Algorithm 1 Iterative Algorithm for Obtaining the LOC-Optimal Transmit Apodization

1: Random Initialization for $\vec{w}_0$
2: **while** $|\|\vec{w}_k\| - 1| > \epsilon$ `and` $\left|\frac{\lambda_k - \lambda_{k-1}}{\lambda_k}\right| > \epsilon$ **do**
3: $\quad \vec{w}_k \leftarrow \vec{w}_k / \|\vec{w}_k\|$
4: $\quad \begin{bmatrix} \vec{w}_{k+1} \\ \lambda_{k+1} \end{bmatrix} \leftarrow \begin{bmatrix} 2A_0 - A_1 - A_{-1} & \vec{w}_k \\ \vec{w}_k^T & 0 \end{bmatrix}^{-1} \begin{bmatrix} \vec{0} \\ 1 \end{bmatrix}$
5: $\quad k \leftarrow k + 1$
6: **end while**
7: **return** $\vec{w}_k$

The constraint on the optimization problem (12) makes it non-convex, so sequential convex programming is used to relax the constraint to $\vec{w}_{prev}^T \vec{w} = 1$, where $\vec{w}_{prev}$ is the solution for $\vec{w}$ from the previous iteration of the same problem after normalizing $\vec{w}$ to a length of 1 (the complete algorithm is shown in Algorithm 1):

$$\begin{aligned} \underset{x}{\text{minimize}} \quad & 2\rho_0 - \rho_1 - \rho_{-1} = \vec{w}^T(2A_0 - A_1 - A_{-1})\vec{w}, \\ \text{subject to} \quad & \vec{w}_{prev}^T\vec{w} = 1. \end{aligned}$$

Figure 1 show the apodization resulting from Algorithm 1 when $N = 128$.

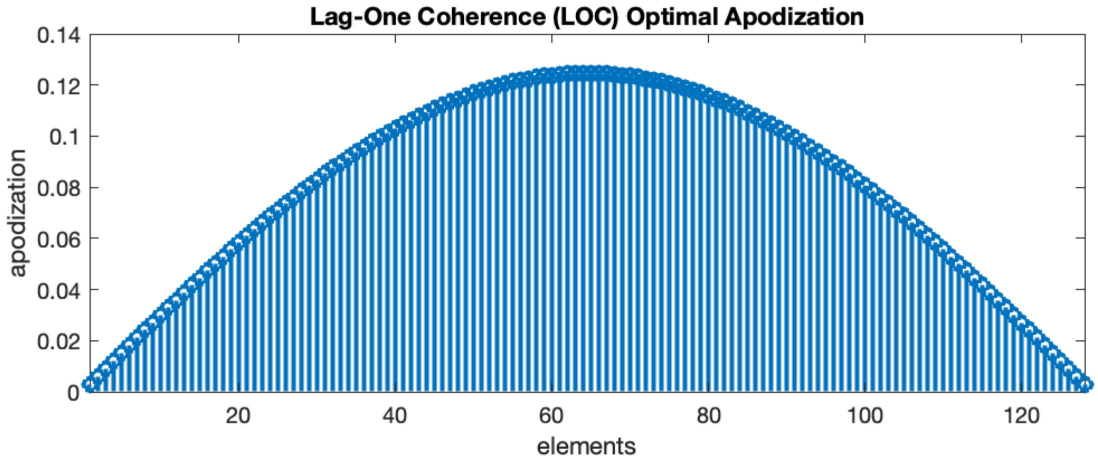

Figure 1. LOC-Optimal Apodization for a 128-Element Aperture Based on Algorithm 1

2.5 Field II Validation of Time-Shift Gather and LOC-Optimal Apodization

Field II[21,22] was used to simulate diffuse scattering at 20 mm depth from a 128-element transducer with 0.2 mm pitch. The transmit pulse had a center frequency of 5 MHz and a 70% fractional bandwidth. The purpose of this initial simulation was to demonstrate agreement between the predicted and actual spatial coherence (functions of lag or element offset) when using either a rectangular apodization or the LOC-optimal apodization. The same diffuse scattering at 20 mm depth was also simulated in the presence of a near-field phase screen. The purpose of this additional simulation was to quickly demonstrate the impact of the LOC-optimal apodization on the time shift gathers and the estimation of aberration delays.

2.6 Reconstruction of Sound Speed from Estimated Delays

The reconstruction of sound speed $c(x,z)$ from estimated delays is a ray tomography problem that uses line integrals over the slowness profile to reconstruct the slowness (i.e., the reciprocal of sound speed):

$$\vec{t}_d = \boldsymbol{DH}\Delta\vec{s}, \tag{14}$$

where $\Delta\vec{s}$ is a vectorization of $\frac{1}{c(x,z)} - \frac{1}{c_{prior}(x,z)}$ (the previous estimate of sound speed is $c_{prior}(x,z)$, so $\Delta\vec{s}$ is an update to $1/c_{prior}$), $\boldsymbol{H}$ is a matrix that encodes line integrals between every transmit element and imaging point, $\boldsymbol{D}$ is a matrix that calculates the differences between the times-of-flight from neighboring transmit elements, and $\vec{t}_d$ is a vector of delay estimates observed between pairs of images I_i and I_{i+1}. The following least-squares problem is used to reconstruct the update $\Delta\vec{s}$ to the slowness image:

$$\min_{\vec{s}} \left\{ \frac{1}{2}(\vec{t}_d - \boldsymbol{DA}\Delta\vec{s})^T \boldsymbol{R}^{-1}(\vec{t}_d - \boldsymbol{DA}\Delta\vec{s}) + \frac{1}{2}\Delta\vec{s}^T \boldsymbol{Q}^{-1}\Delta\vec{s} \right\}, \tag{15}$$

where the residual $\vec{t}_d - \boldsymbol{DA}\Delta\vec{s}$ is modeled as a normal random variable with mean $\vec{0}$ and covariance $\boldsymbol{R}$ (a diagonal matrix whose entries are proportional to the mean path length[11]), and the slowness update image $\Delta\vec{s}$ is modeled as a normal random variable with mean $\vec{0}$ and covariance $\boldsymbol{Q}$ (a Gaussian blurring operator).

2.7 Iterative Sound Speed Estimation and Aberration Correction

We employ an iterative scheme to estimate the speed of sound and correct for phase aberrations in the ultrasound image. Equations (6)-(9) are first used to reconstruct images (initially assuming a spatially constant sound speed) to compute aberration delays. Minimization problem (15) is solved to obtain an update to the speed of sound. This updated sound speed profile is used to recreate the ultrasound image (Figure 2) and compute a new set of aberration delays, which will be used to compute the next update to the speed of sound. This iterative procedure is repeated 10 times to produce the sound speed estimate and aberration-corrected image.

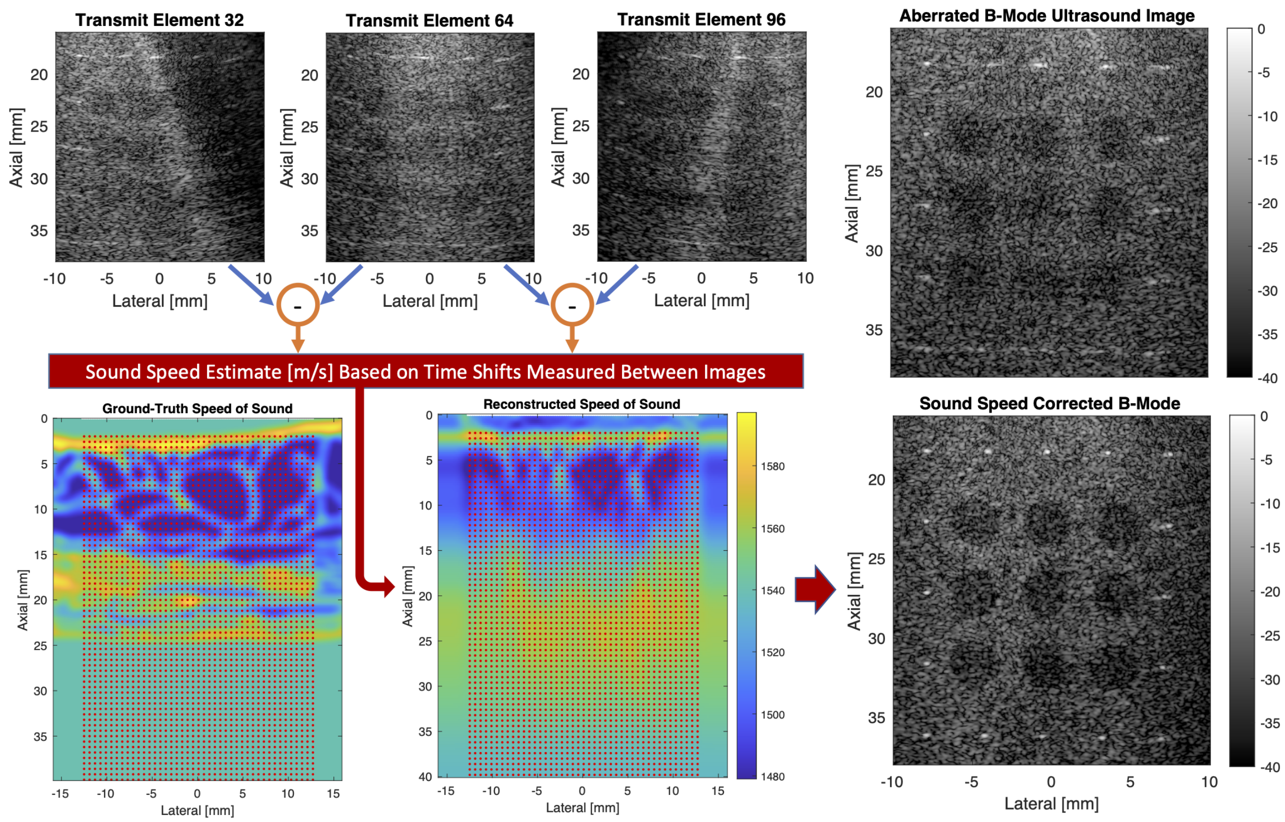

Figure 2. Sound Speed Estimation and Aberration Correction Using Time Shifts Measured Between Reconstructed Images

2.8 Experimental Imaging Studies

All imaging in this study was performed using a Verasonics Vantage 256 ultrasound system (Verasonics Inc., Kirkland, WA, USA) using either an 8 MHz center-frequency L12-5 50mm transducer for *in vitro* phantom studies or a 5 MHz center-frequency L7-4 transducer *in vivo* studies (Advanced Technology Laboratories, Inc., Bothell, WA, USA). Hadamard pulse sequences[23] were used to help generate accurate sound speed estimates in phantoms in order to properly correct for phase aberrations. Experimental demonstrations were performed on multiple *in-vitro* phantoms, whose properties are as described in the next subsection (2.9). Additionally, *in-vivo* datasets were acquired from two healthy and consenting volunteer subjects using the L7-4 transducer per human subjects protocol IRB# 040912M1F. Images of the kidney from subject 1 and gallbladder from subject 2 were acquired for processing.

2.9 Phantom Fabrication

The tissue-mimicking phantom material used in this work was fabricated by cross-linking a mixture of 8% gelatin (Sigma Aldrich, St. Louis, MO, USA), 2.5% silica (US Silica, Katy, TX, USA), 89.4% deionized water, and 0.1% glutaraldehyde (Sigma Aldrich)[24] in a 4-inch acrylic cube. Two (Figure 5, Top) or three (Figure 5, bottom) rows of point targets which consisted of 36-GA (127-μm diameter) wire (McMaster-Carr, Elmhurst, IL) were included as imaging targets within all phantoms. Additionally, hypo-echoic lesions consisting of 8% gelatin, 0.5% silica, 91.4% deionized water, and 0.1% glutaraldehyde (i.e., lower silica content compared to the phantom background)[24] were also included at the distal boundary of some phantoms to provide diversity in imaging targets. In order to create sound speed variation in the near field, gelatin inclusions with an increased sound speed were also cast above the imaging targets by using a mixture of 8% gelatin, 2.5% silica, 69.4% deionized water, 20% isopropanol, and 0.1% glutaraldehyde.[24]

3. RESULTS

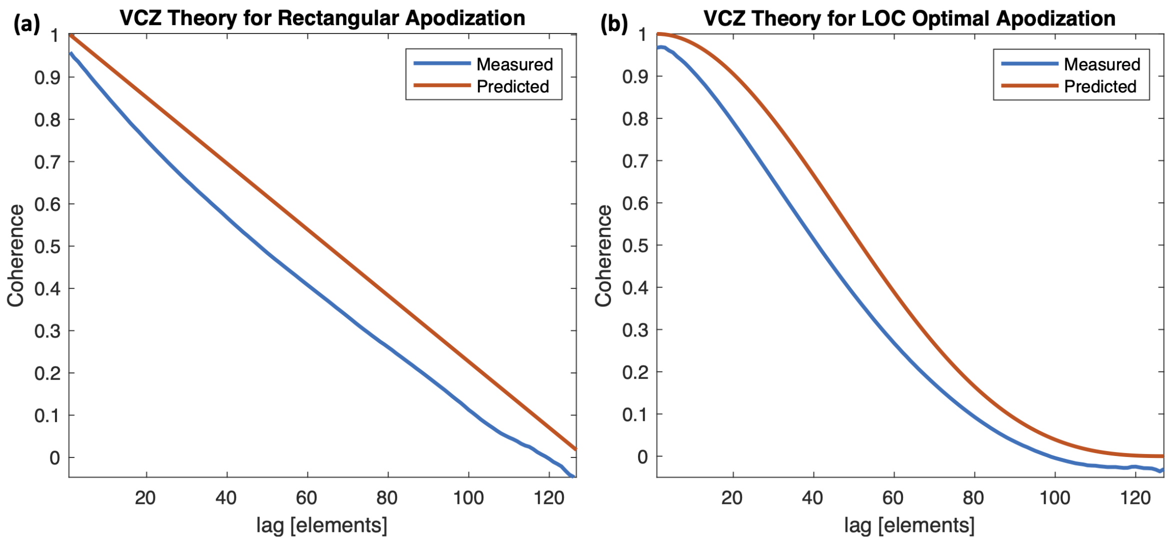

Figure 3. Measured vs. theoretical signal coherence as functions of lag (or element offset) for (a) the rectangular apodization, and (b) the LOC-optimal apodization.

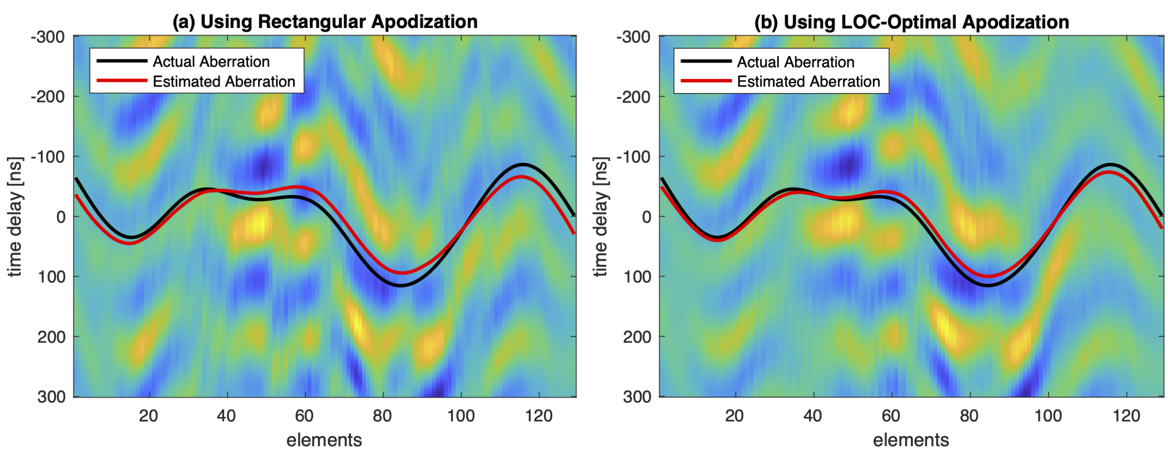

Figure 4. Time-shift gathers using (a) the rectangular apodization and (b) the LOC-optimal apodization for a speckle generating phantom aberrated by a near-field phase screen. The root-mean-square (RMS) error in the aberration delay measurement is 17.1844 ns in (a) and 10.7908 in (b). The LOC-optimal apodization results in the most accurate measurement of aberration delays using the time-shift gather.

The first step in optimizing the aberration delay measurement process was finding the LOC-optimal apodization that would maximize the nearest-neighbor cross-correlation between adjacent element on ultrasound transducer. Figure 1 shows the LOC-optimal apodization for a 128-element transducer. The VCZ theorem is used to predict the spatial coherence as a function of lag (or element offset) for the rectangular and optimal apodizations. Figure 3 experimentally confirms these spatial coherence profiles in a uniform speckle-generating region of a uniform sound speed phantom simulated in Field II.[21,22] Additionally, when a near-field phase screen is applied to this Field II simulation, Figure 4 shows the time-shift gathers resulting from (a) the rectangular apodization and (b) the LOC-optimal apodization. The LOC-optimal apodization increases the smoothness of signals across

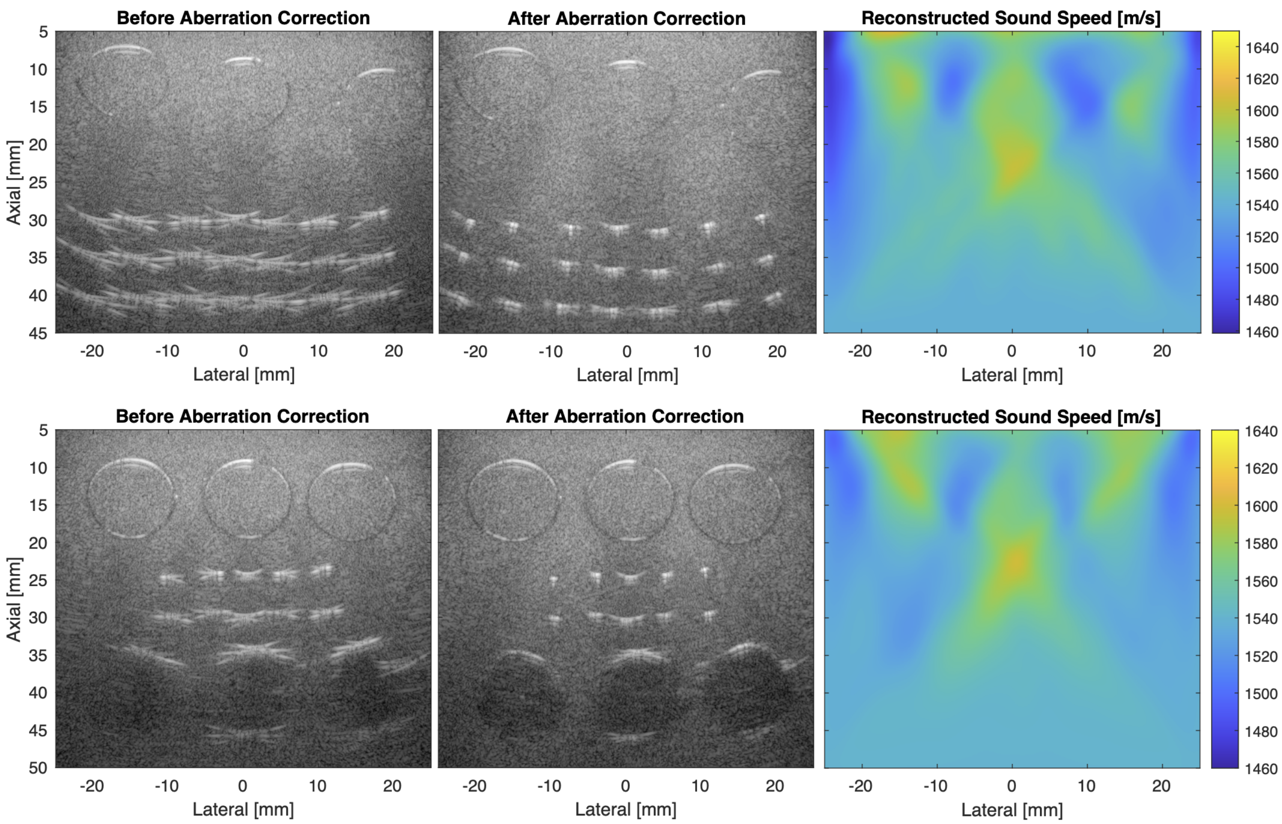

Figure 5. Sound Speed Estimation and Phase Aberration Correction in Phantoms. In the top phantom, three isopropanol-containing inclusions were placed above three rows of seven point targets. In this phantom, the full width at half maximum (FWHM) resolution decreases from 4.7±1.6 mm to 0.9±0.5 mm, which is a 77±17% improvement in point target resolution. In the bottom phantom, three isopropanol-containing inclusions were placed above two rows of five point targets with three anechoic inclusions at the bottom. In this phantom, the FWHM decreases from 2.5±1.8 mm to 0.8±0.7 mm, which is a 58±22% improvement in point target resolution; the contrast in the anechoic inclusions increases from 2.7 ± 1.1 dB to 6.1 ± 1.5 dB; and the contrast-to-noise ratio (CNR) increases from 0.2 ± 0.06 to 0.5 ± 0.09.

the transmit elements in the time-shift gather and improves the accuracy of the aberration delay measurement from 17.2 to 10.8 ns root-mean-square (RMS) error.

We applied time-shift gathers with the LOC-optimal apodization to accurately measure the time delays that were used to estimate the sound speed profile shown in Figure 2. After reconstructing the sound speed profile shown in Figure 2 (which uses k-Wave simulated[25] data) and correcting the aberrations in the B-mode image, we demonstrated this method in phantoms and *in-vivo*.

Accurate tissue-mimicking phantoms were fabricated using the methods described herein, both regarding sound speed and echogenicity. The inclusion of 20% isopropyl alcohol provides a significant increase in sound speed compared to the background material (i.e., greater than 1600 m/s) which causes high levels of aberration in both point targets and hypoechoic targets. Figure 5 shows aberration correction in phantoms based on the estimated speed of sound. In the top and bottom phantoms, the improvement in point target resolution is 77±17% and 58±22%, respectively. In the hypoechoic lesions within the bottom phantom, contrast improves by 3.4 dB and CNR improves by a factor of 2.5.

Figure 6 shows two examples from the abdomen of a healthy human volunteer. There appears to be improved focusing in certain structures within the kidney. In the gallbladder imaging example, we not only see improved visualization of the boundaries of the gallbladder, but we also see the improved focusing of structures from 20

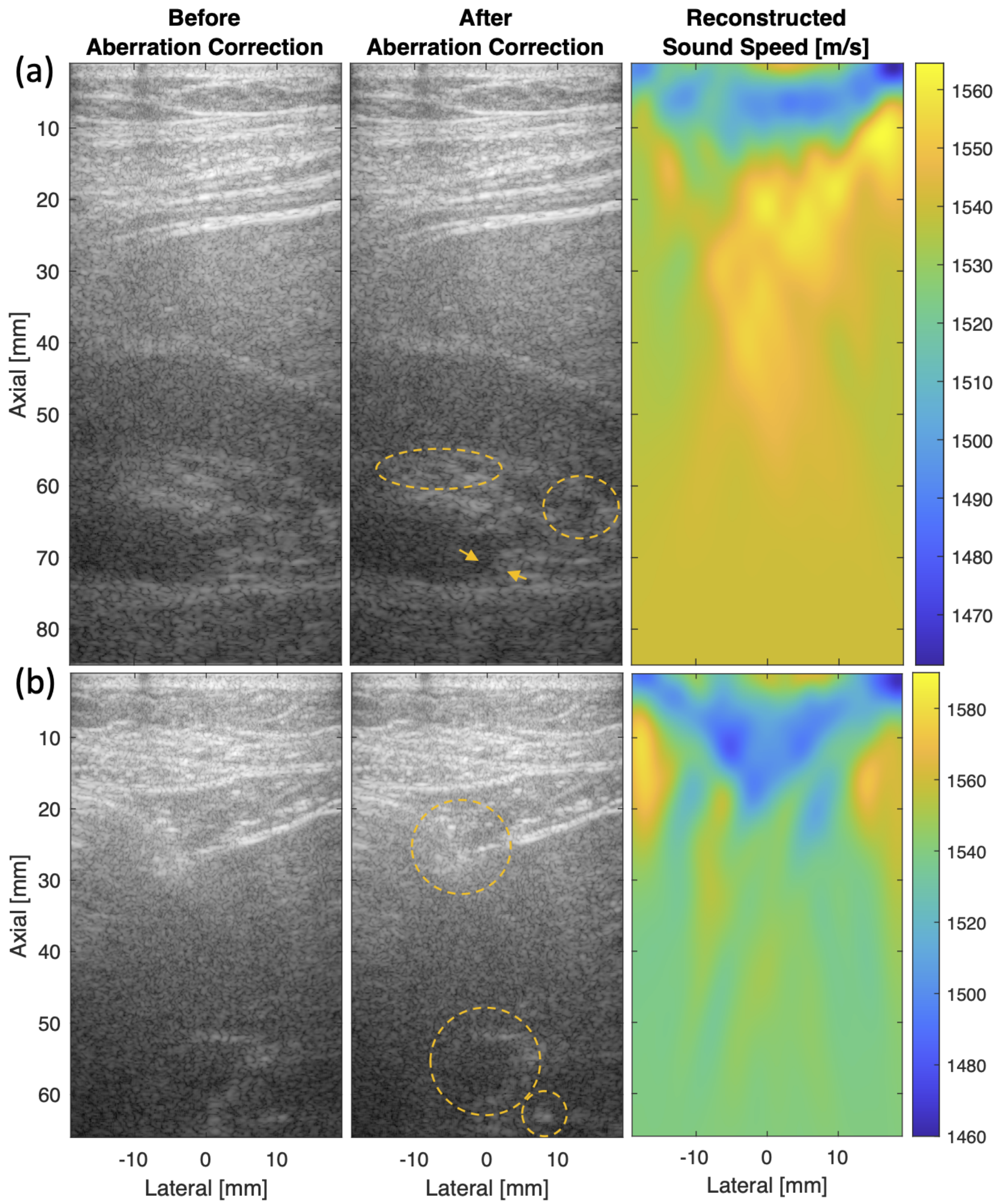

Figure 6. Demonstration of Sound Speed Estimation and Aberration Correction in the Abdomen Using an L7-4 Probe. (a) The focusing of structures within the kidney improve as a result of aberration correction. (b) The focusing of superficial structures from 20 to 30 mm depth and the boundaries of the gallbladder at roughly 55 mm depth improves as result of aberration correction.

to 30 mm depth. Although more severe examples of aberration exist in the human body, the high-frequency probes available to us for raw channel data capture were unable to achieve sufficient SNR at the imaging depths relevant to those examples. Future work will use raw channel data capture capabilities on a clinical scanner to further investigate this technique.

4. DISCUSSION AND CONCLUSIONS

Sound speed estimation in pulse-echo ultrasound is a far more challenging and ill-posed inverse problem than transmission-based ultrasound tomography because of additional ambiguities in the depth placement of the imaging target. With certain exceptions (e.g., assuming a spatially constant or a depth-varying sound speed profile[11,17]), depth placement is ultimately determined by the initial sound speed guess.[15,16] This error in depth placement ultimately biases the final estimate of the average sound speed in the medium. Despite the lack of constraints on the distribution of sound speed in the medium that would allow for an accurate estimate of the average sound speed, the resulting sound speed estimate is often sufficient for aberration correction. This is shown in our work using k-Wave simulation, *in vitro* phantom experiments, and *in vivo* abdominal imaging examples.

An important distinction between the methodology shown here and prior works[9,10] is that the prior work[9,10] generally relies on the conversion of spatial shifts in the image to shifts in time. This approach can be error prone if it does not account for the nonuniform transformation from time to space.[17] The improved model in[9] specifically requires the use of a common mid-angle setup to optimally correlate signals from different propagation paths and make the nonuniform transformation from time to space more explicit: a spatial dilation by the cosine of the half-angle offset between the transmit and receive plane waves. It is much more difficult to apply such a model in our scenario because it involves single-element diverging wave transmits whose angle of transmission (and reception) would be vary with the imaging point. Instead, our approach uses time shift gathers that directly allow us to measure aberration delays without requiring a conversion from spatial shift to time. The other motivation behind the common midangle approach is that signals from different transmit and receive angle pairs within the common midangle gather are optimally correlated. However, this ultimately complicates sound speed tomography by requiring differential measurements of two-way (transmit and receive) times of flight. Our approach reduces the problem back to a one-way (transmit-only) problem by using a fixed receive aperture across all transmit events. However, if we apply an LOC-optimal apodization to the receive aperture, images from neighboring single-element diverging-wave transmissions will be optimally correlated in diffusely scattering medium.

Regardless of the differences between our methodology and the common midangle approach,[9] we reiterate that all pulse-echo sound speed estimators are ultimately subject to the same depth-velocity ambiguities previously mentioned when speed of sound in the medium is not appropriately constrained to homogeneous or layered distribution. A convolutional interpretation of sound speed tomography using the common midangle principle shows[15] shows that the common midangle method is subject to the same depth-velocity ambiguity. Despite improvements in the correlation of signals used to measure the aberration delay and a more accurate conversion from spatial shift to time, the common midangle approach[9] cannot inherently overcome the depth-velocity ambiguity. The use of a calibration phantom to adjust for biases caused by the initial sound speed may explain the apparent lack of dependence on initial sound speed in some of the prior work.[9,26] Our work, motivated by errors in the depth placement of the imaging target caused by the initial sound speed guess, uses an iterative approach that relies on the re-measurement of aberration delays with each new sound speed estimate. Although the iterative approach improves aberration correction, the sound speed estimate appears to remain biased by the initial sound speed guess. Despite this fundamental limitation on sound speed tomography, significant aberration corrections are shown in each result. Future work will consist of a more complete simulation study that explicitly demonstrates that similar aberration correction can be achieved despite differences in the depth placement of the imaging target.

ACKNOWLEDGMENTS

The authors would like to acknowledge Drs. Walter Simson, Anthony Podkowa, and Sergio Sanabria, as well as Electrical Engineering PhD students Thurston Brevett and Louise Zhuang, all from Stanford University, for their many fruitful discussions on the topic of sound speed estimation.

REFERENCES

[1] Li, Y., "Phase aberration correction using near-field signal redundancy. i. principles [ultrasound medical imaging]," *IEEE transactions on ultrasonics, ferroelectrics, and frequency control* **44**(2), 355–371 (1997).

[2] Dahl, J. J., McAleavey, S. A., Pinton, G. F., Soo, M. S., and Trahey, G. E., "Adaptive imaging on a diagnostic ultrasound scanner at quasi real-time rates," *IEEE transactions on ultrasonics, ferroelectrics, and frequency control* **53**(10), 1832–1843 (2006).

[3] Mozaffarzadeh, M., Verweij, M. D., de Jong, N., and Renaud, G., "Comparison of phase-screen and geometry-based phase aberration correction techniques for real-time transcranial ultrasound imaging," *Applied Sciences* **12**(19), 10183 (2022).

[4] Tillett, J. C., Astheimer, J. P., and Waag, R. C., "A model of distributed phase aberration for deblurring phase estimated from scattering," *IEEE transactions on ultrasonics, ferroelectrics, and frequency control* **57**(1), 214–228 (2009).

[5] Liu, D.-L. and Waag, R. C., "Correction of ultrasonic wavefront distortion using backpropagation and a reference waveform method for time-shift compensation," *The Journal of the Acoustical Society of America* **96**(2), 649–660 (1994).

[6] Fink, M., "Time reversal of ultrasonic fields. i. basic principles," *IEEE transactions on ultrasonics, ferroelectrics, and frequency control* **39**(5), 555–566 (1992).

[7] Jaeger, M., Held, G., Peeters, S., Preisser, S., Grünig, M., and Frenz, M., "Computed ultrasound tomography in echo mode for imaging speed of sound using pulse-echo sonography: proof of principle," *Ultrasound in medicine & biology* **41**(1), 235–250 (2015).

[8] Rau, R., Schweizer, D., Vishnevskiy, V., and Goksel, O., "Speed-of-sound imaging using diverging waves," *International Journal of Computer Assisted Radiology and Surgery* **16**(7), 1201–1211 (2021).

[9] Stähli, P., Kuriakose, M., Frenz, M., and Jaeger, M., "Improved forward model for quantitative pulse-echo speed-of-sound imaging," *Ultrasonics* **108**, 106168 (2020).

[10] Rau, R., Schweizer, D., Vishnevskiy, V., and Goksel, O., "Ultrasound aberration correction based on local speed-of-sound map estimation," in [*2019 IEEE International Ultrasonics Symposium (IUS)*], 2003–2006, IEEE (2019).

[11] Ali, R., Brevett, T., Hyun, D., Brickson, L. L., and Dahl, J. J., "Distributed aberration correction techniques based on tomographic sound speed estimates," *IEEE Transactions on Ultrasonics, Ferroelectrics, and Frequency Control* **69**(5), 1714–1726 (2022).

[12] Jiang, C., Li, Y., Li, B., Liu, C., Xu, F., Xu, K., and Ta, D., "Ray theory-based transcranial phase correction for intracranial imaging: A phantom study," *IEEE Access* **7**, 163013–163021 (2019).

[13] Jiang, C., Li, Y., Xu, K., and Ta, D., "Full-matrix phase shift migration method for transcranial ultrasonic imaging," *IEEE Transactions on Ultrasonics, Ferroelectrics, and Frequency Control* **68**(1), 72–83 (2020).

[14] Schwab, H.-M., Ihrig, A., Depke, D., Hermann, S., Schäfers, M., and Schmitz, G., "Aberration correction in photoacoustic imaging using paraxial backpropagation," in [*2017 IEEE International Ultrasonics Symposium (IUS)*], 1–4, IEEE (2017).

[15] Podkowa, A. S. and Oelze, M. L., "The convolutional interpretation of registration-based plane wave steered pulse-echo local sound speed estimators," *Physics in Medicine & Biology* **65**(2), 025003 (2020).

[16] Podkowa, A. S., *Spatiotemporal excitation sequence manipulation and processing for Doppler ultrasound and pulse-echo sound speed imaging applications*, PhD thesis, University of Illinois at Urbana-Champaign (2020).

[17] Ali, R., Telichko, A. V., Wang, H., Sukumar, U. K., Vilches-Moure, J. G., Paulmurugan, R., and Dahl, J. J., "Local sound speed estimation for pulse-echo ultrasound in layered media," *IEEE Transactions on Ultrasonics, Ferroelectrics, and Frequency Control* **69**(2), 500–511 (2021).

[18] Vyas, U. and Christensen, D., "Ultrasound beam simulations in inhomogeneous tissue geometries using the hybrid angular spectrum method," *IEEE transactions on ultrasonics, ferroelectrics, and frequency control* **59**(6), 1093–1100 (2012).

[19] Sava, P. and Fomel, S., "Time-shift imaging condition in seismic migration," *Geophysics* **71**(6), S209–S217 (2006).

[20] Long, W., Bottenus, N., and Trahey, G. E., "Lag-one coherence as a metric for ultrasonic image quality," *IEEE transactions on ultrasonics, ferroelectrics, and frequency control* **65**(10), 1768–1780 (2018).

[21] Jensen, J. A. and Svendsen, N. B., "Calculation of pressure fields from arbitrarily shaped, apodized, and excited ultrasound transducers," *IEEE transactions on ultrasonics, ferroelectrics, and frequency control* **39**(2), 262–267 (1992).

[22] Jensen, J. A., "Field: A program for simulating ultrasound systems," in [*10TH NORDICBALTIC CONFERENCE ON BIOMEDICAL IMAGING, VOL. 4, SUPPLEMENT 1, PART 1: 351–353*], Citeseer (1996).

[23] Harrison, T., Sampaleanu, A., and Zemp, R. J., "S-sequence spatially-encoded synthetic aperture ultrasound imaging [correspondence]," *IEEE transactions on ultrasonics, ferroelectrics, and frequency control* **61**(5), 886–890 (2014).

[24] Cook, J. R., Bouchard, R. R., and Emelianov, S. Y., "Tissue-mimicking phantoms for photoacoustic and ultrasonic imaging," *Biomedical optics express* **2**(11), 3193–3206 (2011).

[25] Treeby, B. E. and Cox, B. T., "k-wave: Matlab toolbox for the simulation and reconstruction of photoacoustic wave fields," *Journal of biomedical optics* **15**(2), 021314 (2010).

[26] Jaeger, M., Stähli, P., Martiartu, N. K., Yolgunlu, P. S., Frappart, T., Fraschini, C., and Frenz, M., "Pulse-echo speed-of-sound imaging using convex probes," *arXiv preprint arXiv:2202.10633* (2022).